Comparing Speckle Imaging Methods

Gregory C. Dente
GCD Associates, 2100 Alvarado NE, Albuquerque NM 87110, (505) 515-7818
gcdente@gmail.com

Michael L. Tilton
Boeing LTS, P.O. Box 5670, Kirtland AFB, NM 87185, (505) 846-5915
michael.tilton@kirtland.af.mil

Andrew P. Ongstad
Air Force Research Laboratory, Directed Energy Directorate,
Kirtland Air Force Base, NM 87185, (505) 853-3207
andrew.ongstad@kirtland.af.mil

Abstract

We will compare speckle imaging reconstruction results for several speckle imaging approaches. [1] In particular, we will compare and contrast four methods: 1) Knox-Thompson, using a hidden phase-finder in the object spectrum phase reconstruction; [2,3] 2) Knox-Thompson, using a phasor-based phase reconstruction; 3) Bispectrum, using only two bispectrum planes; [4] 4) Bispectrum, using four bispectrum planes. In each application of the four approaches, we first calculate the modulus of the object spectrum using a Wiener-Helstrom filter to remove the speckle transfer function. The methods then differ only in their object spectrum phase reconstructions. In the simulations, we will assume that the only aberrations are those introduced by atmospheric turbulence, setting the ratio of the telescope diameter, D, to the Fried Parameter, r_0, equal to ten.[5] Additionally, we assume that the focal-plane detector array is photon-noise limited, the illumination is narrow-band (essentially monochromatic) and the atmosphere is static during the each data frame. First, we will implement all four methods on a simple binary star object at low photon-per-frame light levels. Next, we will apply the methods to complex extended objects.

Introduction

Speckle imaging techniques have been evolving since the fundamental idea was presented almost forty years ago.[1] The critical insight demonstrated how moments of the Fourier transform of an ensemble of short exposures contain information out to the diffraction limit. Many variations on the theme have been implemented, but in all cases, an ensemble of short-exposure images is collected and then post-processed to restore the object. In this presentation, we will compare speckle imaging reconstruction results for several speckle imaging approaches. Specifically, we will compare and contrast four methods: 1) Knox-Thompson, using a hidden phase-finder in the object spectrum

Report Documentation Page

Form Approved
OMB No. 0704-0188

1. REPORT DATE	2. REPORT TYPE	3. DATES COVERED
SEP 2009		**00-00-2009 to 00-00-2009**

4. TITLE AND SUBTITLE	5a. CONTRACT NUMBER
Comparing Speckle Imaging Methods	5b. GRANT NUMBER
	5c. PROGRAM ELEMENT NUMBER
6. AUTHOR(S)	5d. PROJECT NUMBER
	5e. TASK NUMBER
	5f. WORK UNIT NUMBER
7. PERFORMING ORGANIZATION NAME(S) AND ADDRESS(ES) **Air Force Research Laboratory,Directed Energy Directorate,Kirtland AFB,NM,87185**	8. PERFORMING ORGANIZATION REPORT NUMBER
9. SPONSORING/MONITORING AGENCY NAME(S) AND ADDRESS(ES)	10. SPONSOR/MONITOR'S ACRONYM(S)
	11. SPONSOR/MONITOR'S REPORT NUMBER(S)

12. DISTRIBUTION/AVAILABILITY STATEMENT
Approved for public release; distribution unlimited

13. SUPPLEMENTARY NOTES
2009 Advanced Maui Optical and Space Surveillance Technologies Conference, 1-4 Sep, Maui, HI.

14. ABSTRACT
We will compare speckle imaging reconstruction results for several speckle imaging approaches. 1 In particular, we will compare and contrast four methods: 1) Knox-Thompson, using a hidden phase-finder in the object spectrum phase reconstruction; 2,3 2) Knox-Thompson, using a phasor-based phase reconstruction; 3) Bispectrum, using only two bispectrum planes; 4 4) Bispectrum, using four bispectrum planes. In each application of the four approaches we first calculate the modulus of the object spectrum using a Wiener-Helstrom filter to remove the speckle transfer function. The methods then differ only in their object spectrum phase reconstructions. In the simulations, we will assume that the only aberrations are those introduced by atmospheric turbulence, setting the ratio of the telescope diameter, D, to the Fried Parameter, r0, equal to ten.5 Additionally, we assume that the focal-plane detector array is photon-noise limited, the illumination is narrow-band (essentially monochromatic) and the atmosphere is static during the each data frame. First, we will implement all four methods on a simple binary star object at low photonper- frame light levels. Next, we will apply the methods to complex extended objects.

15. SUBJECT TERMS

16. SECURITY CLASSIFICATION OF:			17. LIMITATION OF ABSTRACT	18. NUMBER OF PAGES	19a. NAME OF RESPONSIBLE PERSON
a. REPORT	b. ABSTRACT	c. THIS PAGE			
unclassified	**unclassified**	**unclassified**	**Same as Report (SAR)**	**10**	

phase reconstruction; [2,3] 2) Knox-Thompson, using a phasor-based phase reconstruction; 3) Bispectrum, using only two bispectrum planes and a phasor-based phase reconstruction;[4] 4) Bispectrum, using four bispectrum planes and a phasor-based phase reconstruction. In all applications, we first calculate the modulus of the object spectrum using a Wiener-Helstrom filter to remove the speckle transfer function. The methods then differ only in their object spectrum phase reconstructions.

The first method solves two-dimensional difference equations for the phase using the method described in Reference 3. There, we demonstrate that the object spectrum phase can be decomposed into a regular, single-valued function determined by the divergence of the phase gradient, as well as a multi-valued function determined by the circulation of the phase gradient; this second function has been called the "hidden phase." The standard least-squares solution to the two-dimensional difference equations always misses this hidden phase. Reference 3 develops a solution method that gives both the regular and hidden parts of the object spectrum phase.

The next three methods all use phasor-based phase reconstruction algorithms. Here, in each case, we develop iterative improvement algorithms that rapidly converge to the least-squares-best, two-dimensional phasor array for each object spectrum.

In our applications, we will implement all four methods on a simple binary star object at low photon-per-frame light levels. Then, we will apply the four methods to several complex extended objects, once again varying the photons per frame. In the simulations, we will assume that the only aberrations are those introduced by atmospheric turbulence setting the ratio of the telescope diameter, D, to the Fried Parameter, r_0, greater than or equal to ten.[5] In all cases, we apply each of the methods to aberrated image ensembles of two-hundred short-exposure data frames. In addition, we assume only photon noise in the short exposures while neglecting other noise sources. We will present numerous results, describing the strengths and weaknesses of each of the four methods applied to both simple and extended objects.

Reconstructing the Object Spectrum Modulus

We label the arrays of short-exposure data as

$$d(l;i,j). \tag{1}$$

The index l = 1,2, … R labels the frame, while the next two indices, (i,j), label the pixel in the array. We take a two-dimensional Finite-Fourier-Transform (FFT) on the pixel indices as

$$\tilde{d}(l;m,n) = FFT\{d(l;i,j)\}. \tag{2}$$

The array indices, (*m*, *n*), label the elements of the two-dimensional FFT. The zero spatial frequency point is labeled $(\overline{m},\overline{n})$. We then form the unbiased average [3]

$$C(m,n)=\frac{1}{R}\sum_{l=1}^{R}\left\{\tilde{d}(l;m,n)\,\tilde{d}^{*}(l;m,n)-\tilde{d}^{*}(l;\overline{m},\overline{n})\right\}\equiv\left|\tilde{\Theta}(m,n)\right|^{2}\cdot H(m,n) \tag{3}$$

in which $\left|\tilde{\Theta}(m,n)\right|$ is the modulus of the object spectrum (FFT) and $H(m,n)$ is the speckle transfer function; this can be calculated with a reference star or even calculated analytically. A standard Wiener-Helstrom deconvolution filter then yields an estimate of the modulus-squared of the object spectrum. In the following comparisons, we use the same modulus for each of the four speckle methods; therefore, they only differ in the phase reconstruction methods.

Reconstructing the Object Spectrum Phase

The object spectrum, essentially the FFT of the object, is given by the modulus times the phase factor as

$$\tilde{\Theta}(m,n)=\left|\tilde{\Theta}(m,n)\right|\cdot\exp(i\,W(m,n))\equiv\left|\tilde{\Theta}(m,n)\right|\cdot P(m,n)\quad, \tag{4}$$

in which $W(m,n)$ is the object spectrum phase array and $P(m,n)$ is defined as the object spectrum phasor array. In what follows, we will develop and compare methods that use a Knox-Thompson or Triple-Correlation data base to generate phase estimates. Results for the phase array, W, or phasor array, P, will then complete our estimate of the object spectrum. In each case, prior to applying an inverse FFT to the reconstructed object spectrum, we applied the diffraction-limited optical transfer function for the telescope; this avoids signal-to-noise problems at the higher spatial frequencies.

In the two Knox-Thompson methods, called KTA and KTB, we start by forming the unbiased cross-spectrums from an ensemble of R short exposures

$$\begin{aligned}C_{x}(m,n)&=\frac{1}{R}\sum_{l=1}^{R}\left\{\tilde{d}(l;m,n)\,\tilde{d}^{*}(l;m+1,n)-\tilde{d}^{*}(l;\overline{m}+1,\overline{n})\right\}\\ C_{y}(m,n)&=\frac{1}{R}\sum_{l=1}^{R}\left\{\tilde{d}(l;m,n)\,\tilde{d}^{*}(l;m,n+1)-\tilde{d}^{*}(l;\overline{m},\overline{n}+1)\right\}.\end{aligned} \tag{5}$$

in which we have picked one unit offset in each direction in the FFT; other offsets can easily be analyzed, but the unit offset choice gives the best accuracy on the high-spatial-frequency phase. The ensemble averaging over many realizations of the turbulence-induced phase screens makes the cross-spectrum transfer functions real-valued. [2] Therefore, the turbulence-induced phase errors are averaged away and the phase of the cross-spectrum can be

directly related to phase differences in the object spectrum.[3] The remaining phases of these two cross-spectrums lead to two two-dimensional difference equations for the phase of the object spectrum as

$$C_x(m,n) = |C_x(m,n)| \exp(i V_x) = |C_x(m,n)| P(m,n) P^*(m+1,n)$$
$$C_y(m,n) = |C_y(m,n)| \exp(i V_y) = |C_y(m,n)| P(m,n) P^*(m,n+1) \quad (6)$$

in which the cross-spectrum phases, V_x and V_y are related to the object spectrum phase, *W*, as

$$V_x(m,n) \equiv W(m,n) - W(m+1,n)$$
$$V_y(m,n) \equiv W(m,n) - W(m,n+1). \quad (7)$$

In the first method, KTA, we solve these difference equations directly for both the regular and hidden parts of the object spectrum phase array, $W(m,n)$. This method is detailed in reference 3. There, we find the regular phase by minimizing the error function

$$E \equiv \sum_{m,n} \left\{ \left| V_x(m,n) - W_S(m,n) + W_S(m+1,n) \right|^2 + \left| V_y(m,n) - W_S(m,n) + W_S(m,n+1) \right|^2 \right\} \quad (8)$$

while the hidden part of the phase, the part driven by helical phase around branch points in the object spectrum, is given by

$$W_H(m,n) = \frac{1}{2\pi} \sum_{k,l} \arctan\left[\frac{n-l-.5}{m-k-.5} \right] \left[V_x(k,l+1) - V_x(k,l) - V_y(k+1,l) + V_y(k,l) \right] \quad . \quad (9)$$

Figs. (1a) and (1b) demonstrate the importance of the hidden phase component, with the left-hand reconstruction using only the regular phase, while the right-hand reconstruction uses both the regular and hidden phase components; obviously the hidden phase component is critical.

For the second method, KTB, we once again start with Knox-Thompson data. In this case, we solve for the phasor array by minimizing the least-squares error function given as

$$\mathrm{E} = \sum_{m,n} \left\| C_x(m,n) \right| P(m,n) P^{-1}(m+1,n) - C_x(m,n) \Big|^2 + \sum_{m,n} \left\| C_y(m,n) \right| P(m,n) P^{-1}(m,n+1) - C_y(m,n) \Big|^2 . \quad (10)$$

A variation, with respect to $P(k,l)$, leads to a nonlinear system of equations. These can then be iteratively solved to convergence, yielding a least-squares-best phasor array, $P(m,n)$. This procedure is similar to the method used by Hudgin on phase differences.[6]

In the two bispectrum, or Triple-Correlation methods, referred to as TCA and TCB, we start by forming several sets of the short-exposure ensemble averages defined by

$$\beta(m,n;m',n') = \frac{1}{R}\sum_{l=1}^{R} \left\{ \tilde{d}(l;m,n)\,\tilde{d}(l;m',n')\,\tilde{d}^{*}(l;m+m',n+n') - \textit{noise terms} \right\} , \tag{11}$$

in which (m,n) and range over all spatial frequencies in the object spectrum, while (m',n') are fixed array elements. Each value of the pair (m',n') defines a bispectrum plane.

In TCA, we choose two bispectrum planes defined by $m' = \overline{m}+1$, $n' = \overline{n}$ and $m' = \overline{m}$, $n' = \overline{n}+1$, in which $(\overline{m},\overline{n})$ specifies the zero spatial frequency element in the spectrum. This choice is essentially identical to the unit shift used in Knox-Thompson. Once again, the object spectrum phasor array is taken to minimize the least-squares phasor error given by

$$\begin{aligned} \mathrm{E} = & \sum_{m,n} \left| \left| \beta(m,n;\overline{m}+1,\overline{n}) \right| P(m,n) P(\overline{m}+1,\overline{n}) P^{-1}(m+1,n) - \beta(m,n;\overline{m}+1,\overline{n}) \right|^2 \\ & + \sum_{m,n} \left| \left| \beta(m,n;\overline{m},\overline{n}+1) \right| P(m,n) P(\overline{m},\overline{n}+1) P^{-1}(m,n+1) - \beta(m,n;\overline{m},\overline{n}+1) \right|^2 \end{aligned} \tag{12}$$

Here, once again, the variation, with respect to $P(k,l)$, leads to a nonlinear system of equations. These can then be iteratively solved to convergence, yielding a least-squares-best phasor array, $P(m,n)$.

The construction of TCB is based on four closely-spaced bispectrum planes with $(m' = \overline{m}+1,\ n' = \overline{n})$, $(m' = \overline{m},\ n' = \overline{n}+1)$, $(m' = \overline{m}+2,\ n' = \overline{n})$, and $(m' = \overline{m},\ n' = \overline{n}+2)$. Here, the least-squares phasor error function depends on four bispectrums as

$$\begin{aligned} \mathrm{E} = & \sum_{m,n} \left| \left| \beta(m,n;\overline{m}+1,\overline{n}) \right| P(m,n) P(\overline{m}+1,\overline{n}) P^{-1}(m+1,n) - \beta(m,n;\overline{m}+1,\overline{n}) \right|^2 \\ & + \cdots\cdots + \cdots\cdots \\ & + \sum_{m,n} \left| \left| \beta(m,n;\overline{m},\overline{n}+2) \right| P(m,n) P(\overline{m},\overline{n}+2) P^{-1}(m,n+2) - \beta(m,n;\overline{m},\overline{n}+2) \right|^2 \end{aligned} \tag{13}$$

Once again, the least-squares-best values for the phasor array result from an iterative procedure that minimizes this error.

Reconstruction Results

In the simulations, we will assume that the only aberrations are those introduced by atmospheric turbulence, setting the ratio of the telescope diameter, D, to the Fried Parameter, r_0, equal to ten.[5] We could generalize the simulations to include static and dynamic telescope aberrations. Additionally, we assume that the focal-plane detector array is photon-noise limited, so that we neglect dark-current, as well as read noise. Also, we only process the data on (64X64) pixel elements. We fix the final F/# of the telescope so that the diffraction-limited point-spread-function is approximately two, to three pixels in diameter. In all cases, we used the same speckle-derived modulus, while each phase or phasor reconstructor used the algorithms described for KTA, KTB, TCA and TCB in the last section. In each case, we applied the diffraction-limited optical transfer function for the telescope prior to applying an inverse FFT.

First, we implemented all four methods on a simple binary star object at low photon-per-frame light levels. For each case, we used an ensemble of two hundred short-exposure frames with one hundred photons per frame. Figs. (2a, 2b) show a single frame diffraction-limited binary image with photon noise, as well as the long-term aberrated image. The results for all four speckle methods are shown in Figs. (2c-2f). They are all acceptable reconstructions of the simple binary object.

Next, we implemented all four methods on a simple four-star asterism at low photon-per-frame light levels. For each case, we used an ensemble of two hundred short-exposure frames with five hundred photons per frame. Figs. (3a, 3b) show a single frame diffraction-limited asterism image with photon noise, as well as the long-term aberrated image. The results for all four speckle methods are shown in Figs. (3c-3f). In this case, once again, the methods offered acceptable reconstructions.

Finally, we reconstructed a more complicated and extended object at higher-light levels. We used an ensemble of two hundred short-exposure frames, but increased the photons per frame to ten thousand. Figs. (4a, 4b) show a single-frame, diffraction-limited image with photon noise as well as the long-term aberrated image. The results for all four speckle methods are shown in Figs. (4c-4f). For this extended object, the differences between the four speckle reconstruction approaches are more pronounced, with KTB and the closely related TCA giving the best results and TCB the worst.

Discussion and Conclusion

The examples demonstrated reconstructions on 200 short-exposure frames in the presence of significant turbulence. For simple objects with object spectrums extending out to appreciable spatial frequencies, all of the methods, KTA, KTB, TCA, and TCB can work. For extended objects, with much more compact object spectrums, Triple-correlation methods such as TCB are suspect.[7] Methods that incorporate higher-spatial frequency data by incorporating a large number of bispectrum planes will encounter difficulties, since the extended objects typically have a small object spectrum modulus at the larger spatial frequencies. When we recall that our TCB method only

used four closely-spaced bispectrum planes and is already manifesting problems on an extended object, we can well appreciate how additional bispectrum planes can engender even more reconstruction problems.

Although our Knox-Thompson methods, KTA and KTB, as well as the closely related TCA, worked in these examples and in many other test problems, several questions remain: How will the methods compare when more realistic noise sources and additional telescope aberrations are incorporated into the simulations? How will the methods work on real data? How can we know that our phasor-based error functions, Eqs. (10), (12) and (13), are the best choices? In general, is there a truly optimum speckle reconstruction method, an optimum method for both simple and extended object reconstructions at low-light levels and significant atmospheric aberrations? These questions, along with other evolving issues, should be addressed. Based on the present set of reconstruction results, the phasor-based Knox-Thompson method, KTB, would appear to be close to the optimum method, working well on both simple and extended objects.

References

1. A. Labeyrie, "Attainment of diffraction limited resolution in large telescopes by Fourier analyzing speckle patterns in star images," Astron. Astrophys. **6**, 85-87 (1970).
2. K. T. Knox and B. J. Thompson, "Recovery of images from atmospherically degraded short-exposure photographs," Astron. J. **193**, L45-L48 (1974).
3. G. C. Dente, Speckle Imaging and Hidden Phase, Appl. Opt, vol. 39, No. 10, pg. 1480-1485, 2000.
4. G. R. Ayers, M. J. Northcott and J. C. Dainty, "Knox-Thompson and triple-correlation imaging through atmospheric turbulence," J. Opt. Soc. Am. **5**, 963-985 (1987).
5. D. L. Fried, "Optical resolution through a randomly inhomogeneous medium for very long and very short exposures," J. Opt. Soc. Am. **56**, 1372-1379 (1966).
6. R. H. Hudgin, “Wavefront reconstruction for compensated imaging,” J. Opt. Soc. Am., **67**, 375-378 (1977).
7. C. L. Matson, "Weighted-least-squares phase reconstruction from the bispectrum," J. Opt. Soc. Am. A, **8**, 1905-1913 (1991).

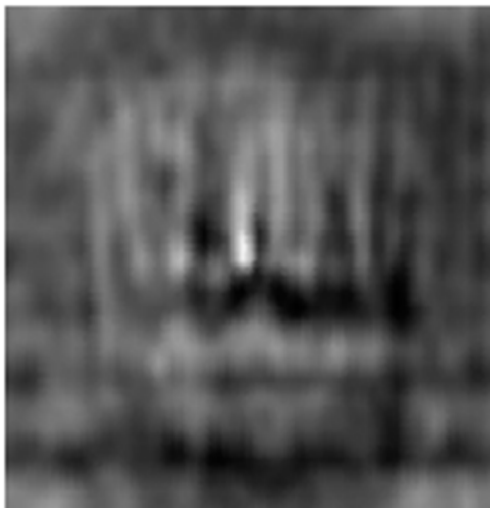

Fig. 1a. Reconstruction without hidden phase.

Fig 1b. Reconstruction with hidden phase.

Fig. 2a. Binary star, diffraction limited image.

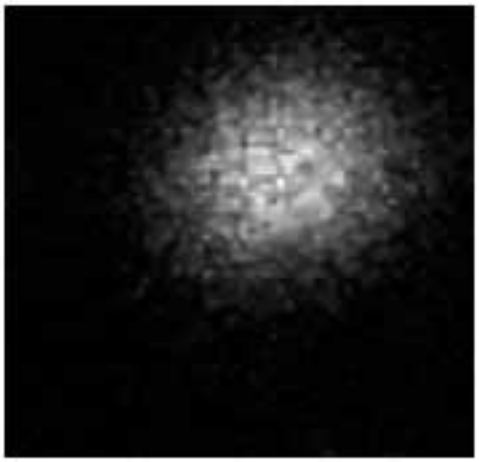

Fig. 2b. Binary star, long term aberrated image.

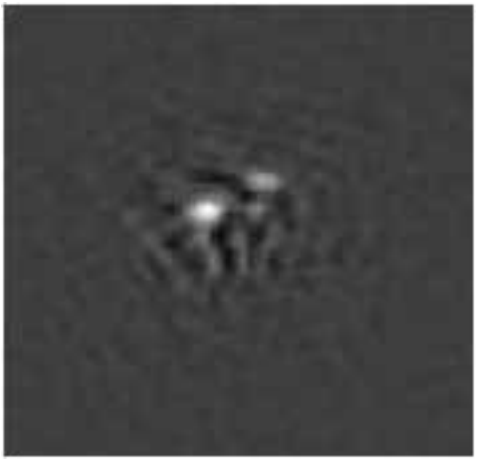

Fig. 2c. Knox-Thompson method A.

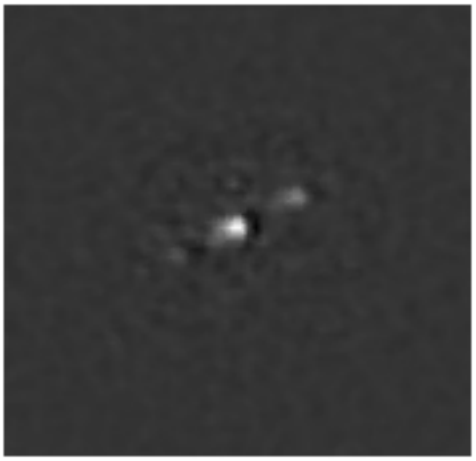

Fig. 2d. Knox-Thompson method B.

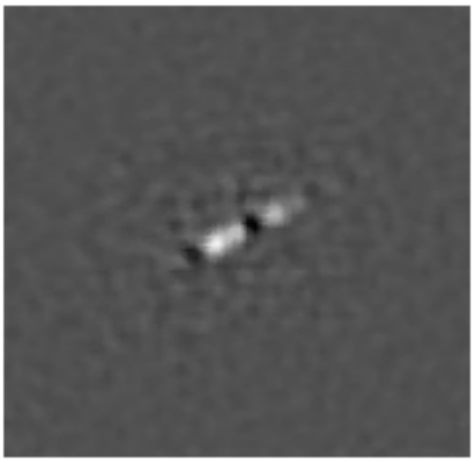

Fig. 2e. Triple-Correlation method A.

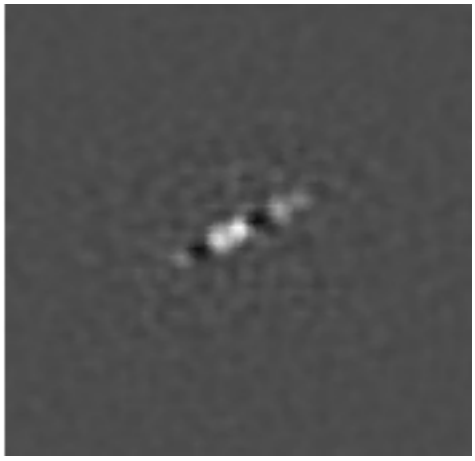

Fig. 2f. Triple-Correlation method B.

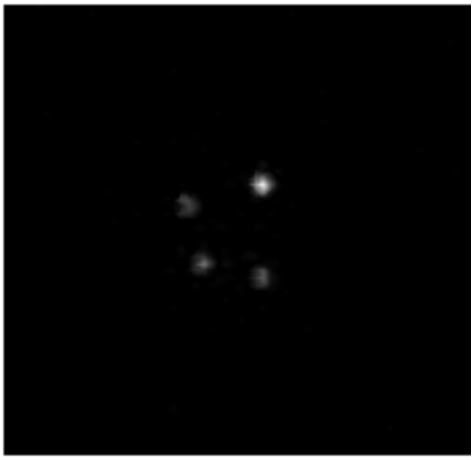

Fig. 3a. Asterism, diffraction limited image.

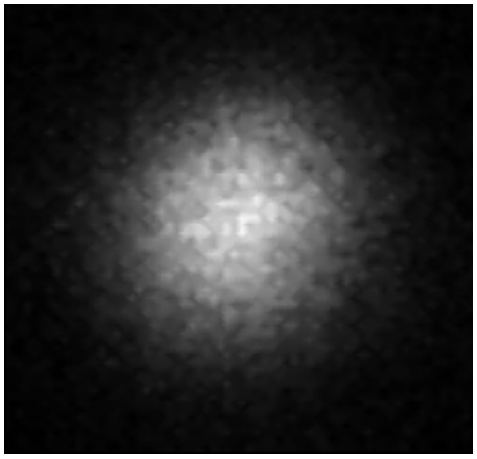

Fig. 3b. Asterism, long term aberrated image.

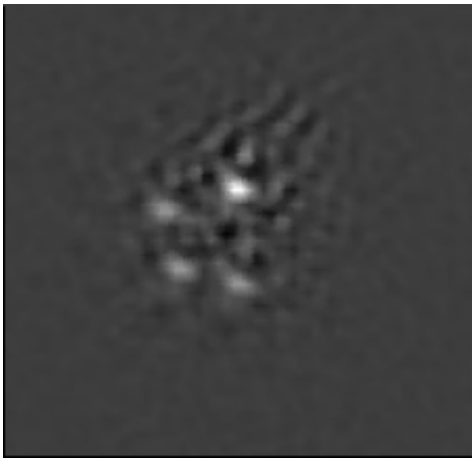

Fig. 3c. Knox-Thompson method A.

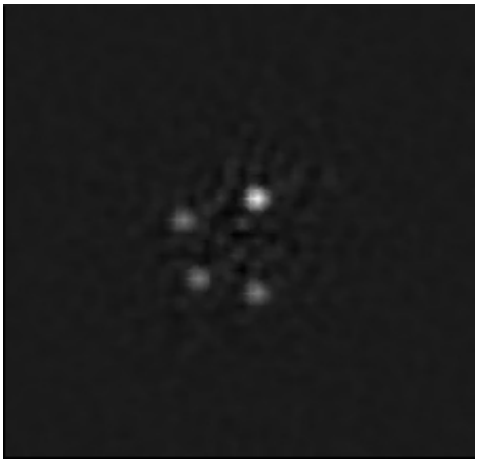

Fig. 3d. Knox-Thompson method B.

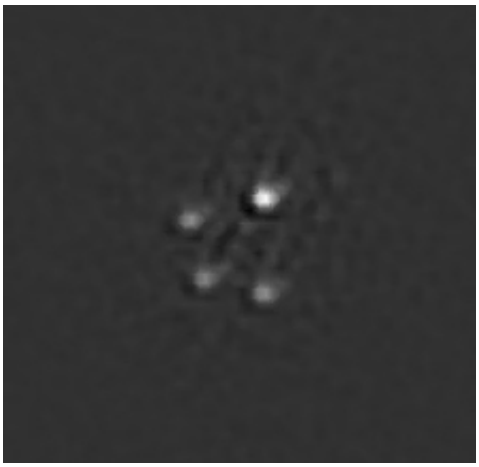

Fig. 3e. Triple-Correlation method A.

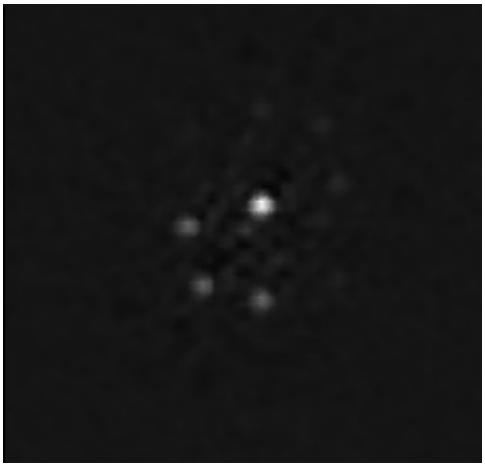

Fig. 3f. Triple-Correlation method B.

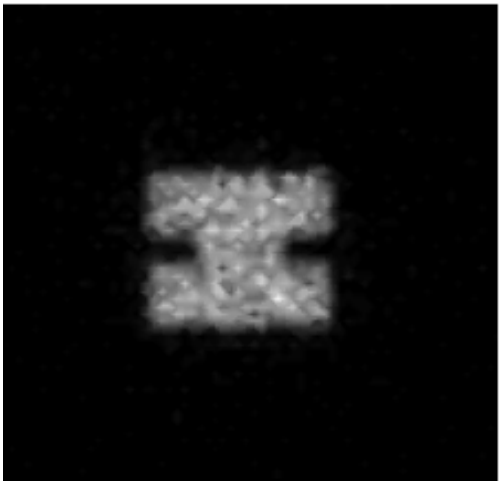

Fig. 4a. Extended object, diffraction limited image.

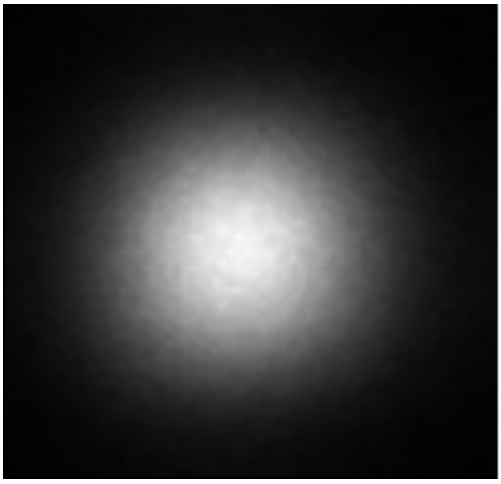

Fig. 4b. Extended object, long term aberrated image.

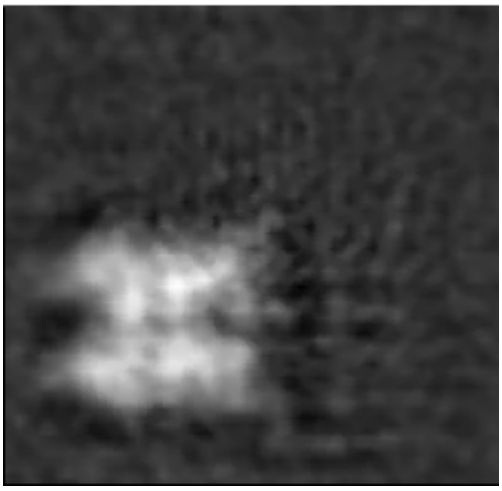

Fig. 4c. Knox-Thompson method A.

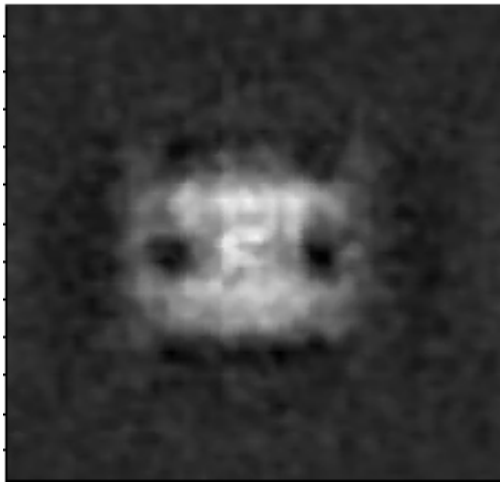

Fig. 4d. Knox-Thompson method B.

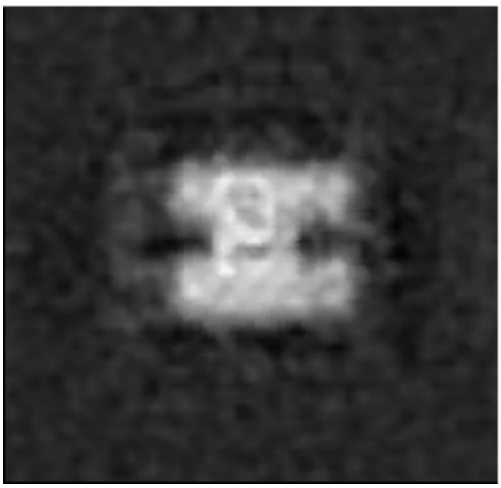

Fig. 4e. Triple-Correlation method A.

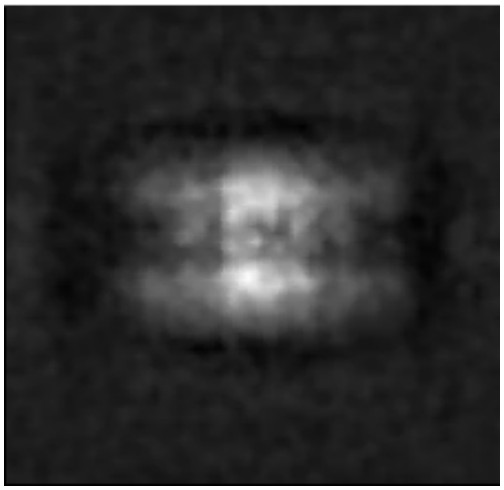

Fig. 4f. Triple-Correlation method B.